

Prediction of crystallographic cracking planes in single-crystal nickel-base superalloys

Christian Busse, Frans Palmert, B. Sjodin, P. Almroth, D. Gustafsson, Kjell Simonsson and Daniel Leidermark

The self-archived postprint version of this journal article is available at Linköping University Institutional Repository (DiVA):

<http://urn.kb.se/resolve?urn=urn:nbn:se:liu:diva-148380>

N.B.: When citing this work, cite the original publication.

Busse, C., Palmert, F., Sjodin, B., Almroth, P., Gustafsson, D., Simonsson, K., Leidermark, D., (2018), Prediction of crystallographic cracking planes in single-crystal nickel-base superalloys, *Engineering Fracture Mechanics*, 196, 206-223. <https://doi.org/10.1016/j.engfracmech.2018.04.047>

Original publication available at:

<https://doi.org/10.1016/j.engfracmech.2018.04.047>

Copyright: Elsevier

<http://www.elsevier.com/>



Prediction of crystallographic cracking planes in single-crystal nickel-base superalloys

C. Busse^{a,*}, F. Palmert^b, B. Sjödin^c, P. Almroth^c, D. Gustafsson^c,
K. Simonsson^a, D. Leidermark^a

^a*Division of Solid Mechanics, Linköping University, SE-58183 Linköping, Sweden*

^b*Division of Engineering Materials, Linköping University, SE-58183 Linköping, Sweden*

^c*Siemens Industrial Turbomachinery AB, SE-61283 Finspång, Sweden*

Abstract

The inherent anisotropy of single-crystal nickel-base superalloys brings many difficulties in terms of modelling, evaluation and prediction of fatigue crack growth. Two models to predict on which crystallographic plane cracking will occur is presented. The models are based on anisotropic stress intensity factors resolved on crystallographic slip planes calculated in a three-dimensional finite-element context. The developed models have been compared to experiments on two different test specimen geometries. The results show that a correct prediction of the crystallographic cracking plane can be achieved. This knowledge is of great interest for the industry and academia to better understand and predict crack growth in single-crystal materials.

Keywords: Single-crystal nickel-base superalloys, Anisotropy, Fracture mechanics, Stress intensity factor, Crystallographic cracking

*Corresponding author

Email address: christian.busse@liu.se (C. Busse)

Nomenclature

C_{11}, C_{12}, C_{44} material stiffness parameters

K_I, K_{II}, K_{III} Mode I, II and III stress intensity factor

Q, N, μ, λ functions of the material properties

R_σ stress ratio

S material compliance matrix

\mathbf{b} slip direction unit vector (Burgers' vector)

\mathbf{n} slip plane normal unit vector

\mathbf{s} evaluation direction unit vector

\mathbf{t} unit vector orthogonal to \mathbf{s} and \mathbf{n}

k_I, k_{II}, k_{III} resolved Mode I, II and III stress intensity factor

k_{EQ} equivalent resolved stress intensity factor

r distance from crack front in x-y plane

r' distance from crack front in arbitrary direction

x, y, z cartesian coordinates

α crystallographic slip system

η_1, η_2, η_3 angle between the projection of the dendrites and the vertical axis of the global coordinate system

γ' strengthening precipitates

γ, β, ϕ angle between crack front coordinate axis and r'

ψ calibration parameter

σ stress tensor

$\zeta_1, \zeta_2, \zeta_3$ angle between the projection of the dendrites and the horizontal axis of the global coordinate system

1. Introduction

In today's world, gas turbines are crucial in the energy generation sector, as their start-up and shut-down times are relatively short, making them perfect candidates for balancing the power grid with respect to inherently intermittent renewable energy sources like wind and solar power [1]. However, more pronounced cyclic loading conditions mean an increased risk for fatigue (primarily thermomechanical fatigue) in critical components. Furthermore, gas turbines are designed to work with very high gas temperatures in order to achieve a good thermal efficiency [2], as increasing the gas temperature in power generating gas turbines lowers the fuel consumption; therefore also lowering costs and reducing pollution [3]. These high temperatures result in high requirements on the materials in the hottest regions. One of the critical regions in a gas turbine is the first turbine stage, where the highest temperatures are present for rotating parts. The turbine blades in this region are often cast in single-crystal form of nickel-base superalloys due to their excellent properties at high temperatures.

The complex material behaviour of single-crystal nickel-base superalloys, like the elastic and plastic anisotropy, makes the modelling of these materials rather complicated. It has been shown that the anisotropy, which is closely linked to the crystallographic structure, has a considerable impact on the yield [4, 5], low-cycle fatigue [6, 7], thermomechanical fatigue [8–10] and creep behaviour [11, 12], to mention a few examples. Thus, the crystallographic structure needs to be accounted for in the modelling context. The same holds true for the fracture mechanical behaviour, where the distinct crystallographic slip planes are potential critical planes for crack initiation [13] and crack growth. Antolovich *et al.* [14] observed that nickel-base superalloys in single-crystal form show two distinct types of fracture. The first one is characterised by fracture on the $\{111\}$ -planes, where the γ' -precipitates are sheared. The second fracture type is characterised by cracking normal to the loading direction, *i.e.* Mode I, and shows a microscopically rough surface, where the crack tends to avoid the γ' -precipitates instead of shearing them.

Fatigue cracks in single-crystal nickel-base superalloys tend to switch from Mode I to crystallographic cracking, where the crack grows along one of the internal crystallographic slip planes [15–18]. Insufficient knowledge of how to handle the crystallographic cracking behaviour leads to large safety margins and conservative designs, which in turn decreases efficiency. Hence, it is important to establish a parameter describing the crack driving force in these materials that accounts for the observed behaviour. Furthermore, the transition from Mode I to crystallographic cracking is also important, as the latter is associated with a higher crack propagation rate [19].

Previous research [16, 20–22] points out the importance of the crystallographic orientation, including the misalignments, as the deviation from the ideal crystallographic orientation, formed during the casting process, has a non-negligible influence on the stress distribution, and thus on the mechanical behaviour and fatigue life. This is important for the industry, where the crystallographic orientations in single-crystal components at stress raising features are generally unknown, due to the rarely controlled secondary orientation in the casting process. Different fracture mechanics approaches for single-crystal superalloys are available in the literature, where Resolved Shear Stresses (RSSes) are commonly used in single-crystal crack growth modelling applications [15, 23, 24]. Telesman and Ghosn [18], as well as Gell and Leverant [25], proposed that the RSSes on the respective crystallographic slip plane can be used to predict the crystallographic fracture plane. Telesman and Ghosn [18] presented an octahedral stress intensity factor parameter that couples a Resolved Shear Stress Intensity Factor (RSSIF) with a Resolved Stress Intensity Factor (RSIF) based on the normal stress acting on the corresponding slip plane. Their work and most of the previous research was done in terms of two-dimensional (2D) analyses, due to its simpler nature. Tinga [15], Ranjan and Arakere [26] and Qiu *et al.* [27] presented frameworks with RSSIFs in a three-dimensional (3D) context based on the anisotropic Stress Intensity Factors (SIF) derived by Sih *et al.* [28]. However, these anisotropic SIFs are restricted to the special case where locally the plane perpendicular to the crack front must

be a plane of material symmetry. This is not valid for most crack front shapes or when a deviation from the ideal crystallographic orientation is present.

Another approach was proposed by Sabnis *et al.* [29], where a microdamage model is used to predict the crack initiation and crack growth. The anisotropic continuum damage mechanics model couples crystal plasticity with damage induced on the crystallographic planes and predicts a realistic crack path in a four-point bending specimen. However, they state that their constitutive model is insufficient for a quantitative comparison with experiments.

In this paper, two different models are presented and evaluated in order to find a reliable prediction of the first global crystallographic cracking plane. The models include the calculations of anisotropic SIFs resolved on the crystallographic planes in a 3D context for arbitrary crack front shapes and crystallographic orientations based on the work of Hoenig [30]. An equivalent RSIF parameter is proposed based on these anisotropic SIFs, which is used to predict the active global crystallographic cracking planes after a transition from Mode I cracking. Validation of the models has been done by isothermal crack growth testing at 500°C for two different specimen geometries, where the crystallographic misalignments, due to the casting procedure, have been taken into account. Furthermore, no fatigue crack growth rate data is presented or used in this work.

The presented methodology is applicable to arbitrary 3D Finite-Element (FE) simulation contexts and crystallographic orientations. This aspect is of high importance for industrial applications, where a physical-inspired model, such as this, can be used to more accurately predict the crack growth in single-crystal components, and thus increase the efficiency of the design as well as the maintenance intervals. The authors are not aware of similar research using 3D-calculations of RSIF parameters based on anisotropic SIFs for arbitrary crack front shapes and crystallographic orientations.

2. Material and Experiments

2.1. Material

The investigated material is a single-crystal nickel-base superalloy of face-centred cubic structure (FCC) developed by Siemens Industrial Turbomachinery AB, similar to the alloy described by Reed *et al.* [31]. Its main alloying elements, in order of decreasing wt%, are as follows: Ni-Cr-Ta-Co-Al-W-Mo-Si-Hf-C-Ce.

As the specimens are cast in only one single grain they possess anisotropic properties, where the elastic stiffness constants for 500 °C are presented in Table 1. The temperature of 500 °C has been chosen since it corresponds to the temperature during normal operation at the blade fir tree root, which is a critical location in the blade design.

Table 1: Elastic stiffness constants, units in GPa.

Temp. (°C)	C ₁₁	C ₁₂	C ₄₄
500	201.9	127.0	112.8

2.2. Experimental procedure

To study the crack growth behaviour and its effects on the studied single-crystal nickel-base superalloy material, a number of isothermal fatigue crack growth experiments at 500 °C were performed. Two different test specimens were investigated in this study; a Disc-shaped Compact Tension (DCT) specimen and a surface flawed fatigue crack growth specimen of Kb-type [32], which henceforth will be denoted as the Kb specimen. The geometry of the two specimens can be seen in Fig. 1. The testing process can be divided into four stages; a flaw introduction by electro discharge machining (EDM), precracking to initiate the crack growth, Mode I crack growth and, finally, transition to crystallographic crack growth. In addition, as stated earlier, no fatigue crack growth rate data will be presented or used in this work. Such data for the DCT specimens can be seen in the work by Palmert *et al.* [33], which describes the testing.

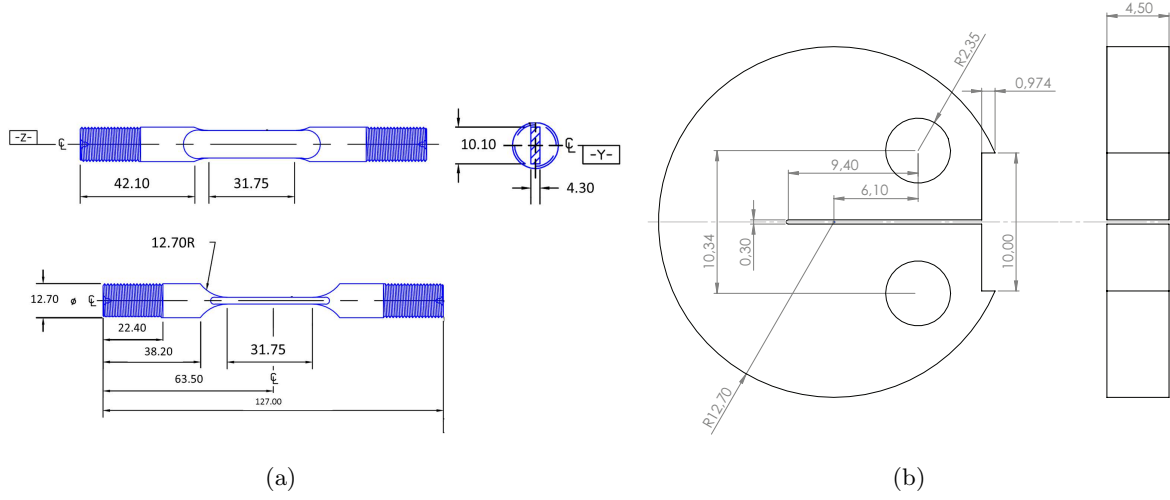


Figure 1: Technical drawing of (a) the Kb specimen and (b) the DCT specimen with dimensions in mm.

2.2.1. Kb specimen

Fatigue crack growth testing of four surface flawed Kb specimens was done according to the guidelines provided in the ASTM E647 [34] test specification. These specimens were manufactured from cast bars with the casting direction parallel to the nominal [001] crystallographic direction. The secondary orientation was orthogonal to the surface flaw. The latter was introduced by EDM as a semi-circular surface flaw centred on one of the large flat surfaces of the specimen gauge section. The depth and width of the EDM-notch was 0.127 mm and 0.245 mm, respectively. The tests were run in an MTS servo-hydraulic testing machine with a test capacity of 89 kN. The test specimens were precracked at room temperature, with a frequency of 10 Hz. After this, the fatigue crack growth tests were performed according to the test conditions shown in Table 2. The crack length was monitored using direct current potential drop measurement (DCPD) according to [35]. After the precracking the crack grew as a Mode I crack up to the transition crack length, except for the specimens Kb2 and Kb3, where the transition to global crystallographic crack growth could be observed directly after the precrack.

Table 2: Overview of the test conditions in the experiments of the Kb specimens.

Specimen	Kb1	Kb2	Kb3	Kb4
Temperature [°C]	500	500	500	500
Stress ratio R_σ [-]	0.05	0.05	0.05	0.05
Frequency [Hz]	0.5	0.5	0.5	0.5
Max. Force [N]	19857	25400	16574	15858
Nominal loading direction	[001]	[001]	[001]	[001]

2.2.2. DCT specimen

Fatigue crack growth testing was conducted on four DCT specimens according to ASTM E647 [34]. These were run in a 100 kN Zwick servo-electric tensile testing machine (Kappa 50DS), with a three-zone furnace. The specimens had an EDM starter notch and were fatigue precracked at room temperature. During the precracking, the displacement over the gauge length was measured using a clip gauge extensometer and the crack length was determined by the compliance method described in ASTM E647. The fatigue crack growth tests were performed according to the test conditions shown in Table 3, with a 30 s hold time at maximum load in each cycle in order to have enough time to gather sufficient measurement data. This is due to software restrictions of the testing machine. After the precracking, the clip gauge extensometer was removed and the crack length was monitored using DCPD according to [35]. The specimens were manufactured from cast bars with the casting direction parallel to the [001] direction. The [001] direction is in the thickness direction of all specimens. The secondary crystal orientation is aligned with the notch, and is [100] for DCT1 and DCT2, [210] for DCT3 and [110] for DCT4, *cf.* Fig. 2. Thus, the nominal loading direction of the specimens are [010], [010], $[\bar{1}20]$ and $[\bar{1}10]$, respectively. For a more in-depth description of the DCT specimen testing see [33].

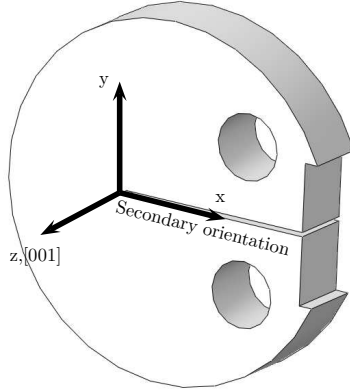


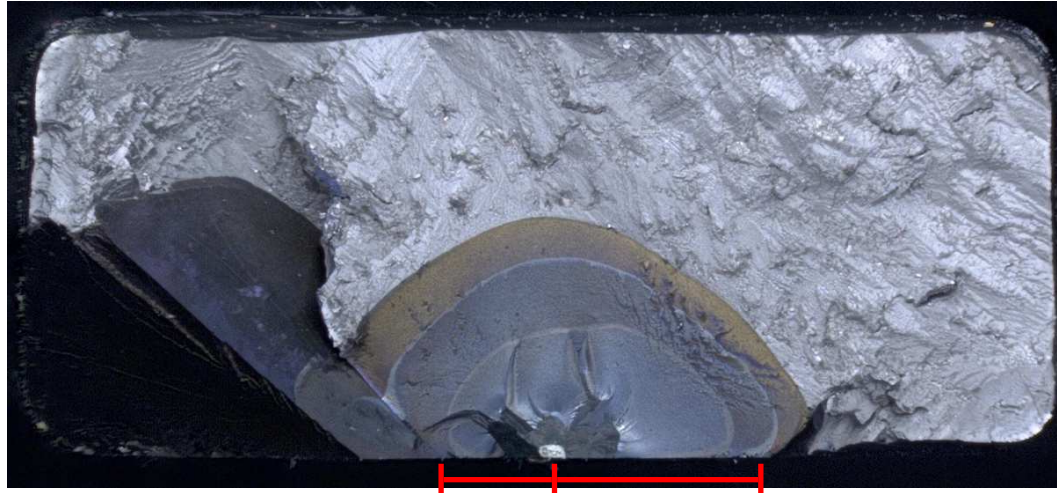
Figure 2: Model of the DCT specimen with the representation of the crystal orientation relative to the global FE-coordinate system.

Table 3: Overview of the test conditions in the experiments of the DCT specimens.

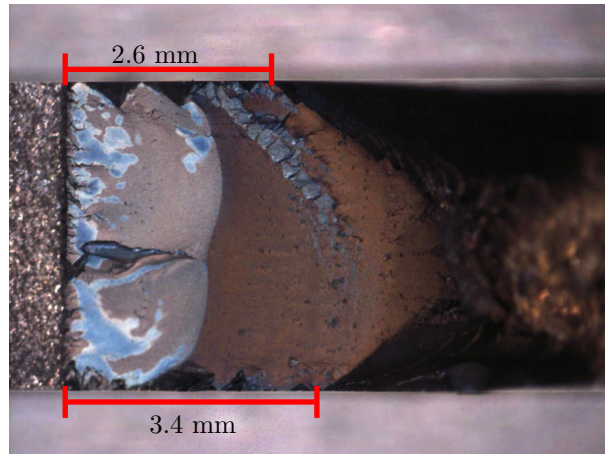
Specimen	DCT1	DCT2	DCT3	DCT4
Temperature [°C]	500	500	500	500
Stress ratio R_σ [-]	0.1	0.1	0.1	0.1
Frequency [Hz]	0.0254	0.0254	0.0254	0.0254
Max. Force [N]	911	658	871	911
Nominal loading direction	[010]	[010]	$[\bar{1}20]$	$[\bar{1}10]$

2.3. Fracture surfaces

After finishing the testing, the fracture surfaces were examined in an optical microscope to determine the crack lengths when the cracking mode switched from Mode I to crystallographic crack growth, as initially a Mode I crack is present in every specimen. From the fracture surfaces it could be observed that each crack grew a distance as a Mode I crack after the precracking until transitioning to global crystallographic cracking, except in the Kb2 and Kb3 specimens where the cracks transitioned directly after the precracking. The transition crack lengths were measured from the center of the EDM notch for the Kb specimens, and for the DCT specimens at the specimen surfaces, see



(a)



(b)

Figure 3: Measurements of the transition crack lengths on the fracture surface of the (a) Kb4 and the (b) DCT1 specimen.

Fig. 3 for examples of these transition crack length measurements. It should be noted, that these measurements are from the optical microscopy examinations and not from DCPD measurements. This procedure was done for all Kb and DCT specimens and the results are summarised in Table 4, where the plane on

which crystallographic crack growth occurred first is marked with an asterisk. It should also be noted, that some local crystallographic crack growth is visible even for crack lengths shorter than the transition crack length, *i.e.* during the precracking and at the free surfaces. This can be seen in Fig. 3, where the Mode I crack surfaces are tortuous at these instances. This points towards crystallographic crack growth on two conjugate slip planes on a microscopic level [14, 36]. No consideration is taken to the local crystallographic cracking, since the crack switches back to Mode I crack growth, and global crystallographic cracking is only observed after the transition crack length is reached. In the areas where the crack grew orthogonal to the loading direction, it can be seen in a higher magnification Scanning Electron Microscope (SEM) image, *cf.* Fig. 4, that the γ' -particles have not been sheared and the crack grew in the γ -matrix. Anotolovich *et. al* [14] proposed that the cracks in the matrix propagate by monotonic cleavage events or as a series of microcracks on the crystallographic planes. The magnification of the SEM image is not high enough to conclude which holds true. Regardless, as the crack avoided the γ' -particles and grew in the interface, considering the context of this work, which is from an engineering point of view, the cracking mode which is perpendicular to the loading direction is macroscopically regarded as a Mode I crack.

Table 4: Global crystallographic cracking planes and the maximum K_I value along the crack front at the first transition of the crack.

Specimen	Kb1	Kb2	Kb3	Kb4	DCT1	DCT2	DCT3	DCT4
Left cracking plane	$\bar{1}1\bar{1}^*$	$\bar{1}1\bar{1}^*$	$\bar{1}1\bar{1}^*$	$\bar{1}1\bar{1}^*$	$1\bar{1}\bar{1}$	$1\bar{1}\bar{1}$	$1\bar{1}\bar{1}^*$	no crystallographic cracking
Transition crack length left [mm]	0.95	0.1225(direct)	0.1225(direct)	1	3.4	3.5	2.4	no crystallographic cracking
Right cracking plane	$\bar{1}\bar{1}1$	$\bar{1}\bar{1}1$	$\bar{1}\bar{1}1$	$\bar{1}\bar{1}1$	$\bar{1}\bar{1}1^*$	$\bar{1}\bar{1}1^*$	$\bar{1}\bar{1}1$	no crystallographic cracking
Transition crack length right [mm]	1	0.85	0.9	2.1	2.6	3.1	3.6	no crystallographic cracking
Max. K_I at transition crack length [$\text{MPa}\sqrt{\text{m}}$]	19.5	9.13	5.9	15.6	33.1	37.8	22.2	no crystallographic cracking

*first active crystallographic slip plane

For the Kb specimens, the shape of the growing crack can be seen due to heat tinting during the testing, *cf.* Fig. 3a, and can be approximated to be semi-circular. No heat tinting was done in the testing of the DCT specimens

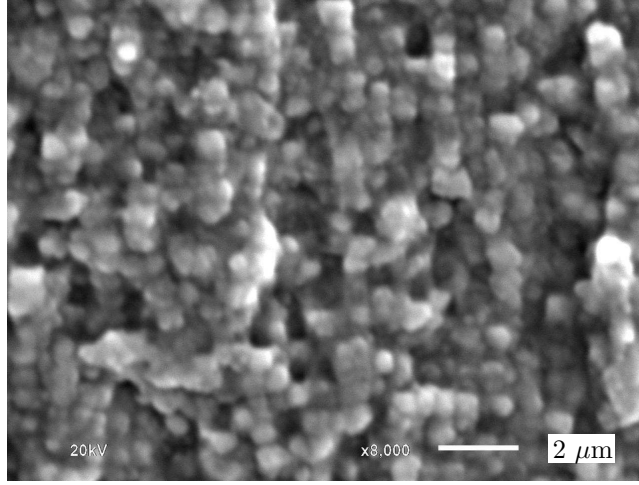
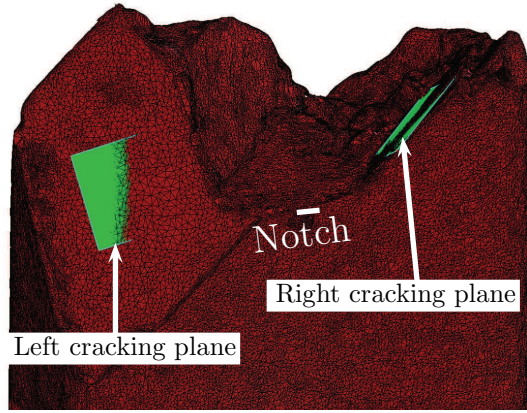


Figure 4: SEM image of the Mode I fracture surface of the specimen DCT1 at a length of approximately 2 mm from the notch in the center of the specimen.

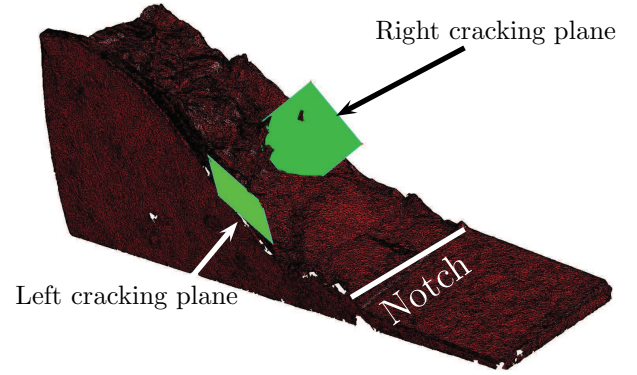
and therefore semi-elliptical crack front shapes with a shallow depth have been assumed.

The fracture surfaces of the specimens were also scanned in an Atos Triple Scan machine to acquire a 3D representation of the fracture surfaces in terms of mesh data. These were imported to an FE-preprocessor, where planes with the corresponding normals to the $\{111\}$ -planes were added for visualisation. This is a convenient procedure to identify the crystallographic plane on which the crystallographic crack grew.

In Fig. 5 the scanned fracture surfaces of the Kb1 and DCT1 specimens are depicted, where the EDM notches and the two obtained crystallographic cracking planes are highlighted. This was done for all Kb and DCT specimens and the results are summarised in Table 4, which also shows the maximum K_I values along the crack front at the transition crack length in order to establish a comparison between the specimens. The calculation of the K_I values is described below. From this evaluation it could be seen that the DCT4 specimen does not show any crystallographic cracking. The scanned fracture surface of DCT4 is shown in Fig. 6a, containing the visualised $(1\bar{1}\bar{1})$ -plane, which inter-

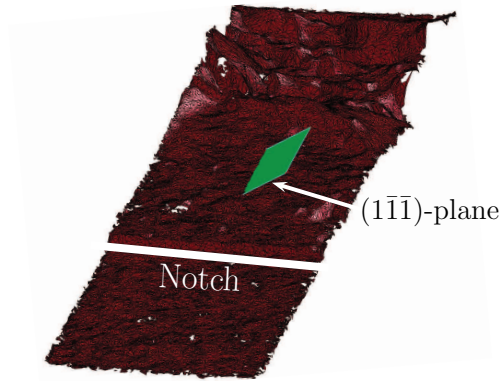


(a)

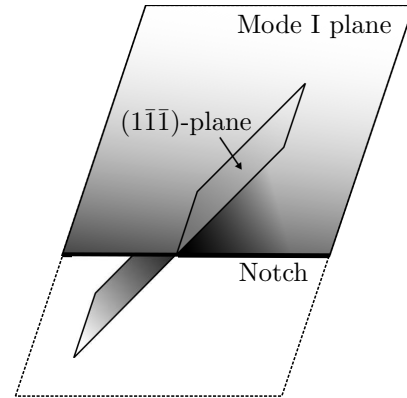


(b)

Figure 5: The scanned fracture surface of (a) Kb1 and (b) DCT1 with visualised crystallographic cracking planes.



(a)



(b)

Figure 6: (a) Scanned fracture surface of DCT4 with visualized $(1\bar{1}\bar{1})$ -plane and (b) a schematic representation of the intersection of the Mode I cracking plane with the $(1\bar{1}\bar{1})$ -plane.

sects the fracture surface exactly parallel to the crack growth direction. Fig. 6b illustrates this schematically in order to visualise the location of the $(1\bar{1}\bar{1})$ -plane in relation to the Mode I cracking plane. The importance of this particular crystallographic slip plane is further discussed in Section 6.

2.4. Crystallographic orientation and misalignments

The importance of the crystallographic orientation and misalignments has been pointed out earlier. On each specimen, three orthogonal faces were polished and etched. The dendrites visible on these surfaces represent the projection of the crystallographic lattice vectors in the vertical and horizontal directions; *cf.* Fig. 7a where some are highlighted. The angles between each visible dendrite projection and the vertical and horizontal axis of each surface relative to the global coordinate system were measured. This is schematically shown in Fig. 7b in terms of a cube representing the three orthogonal faces, where the angles $\zeta_{1,2,3}$ and $\eta_{1,2,3}$ are quantified.

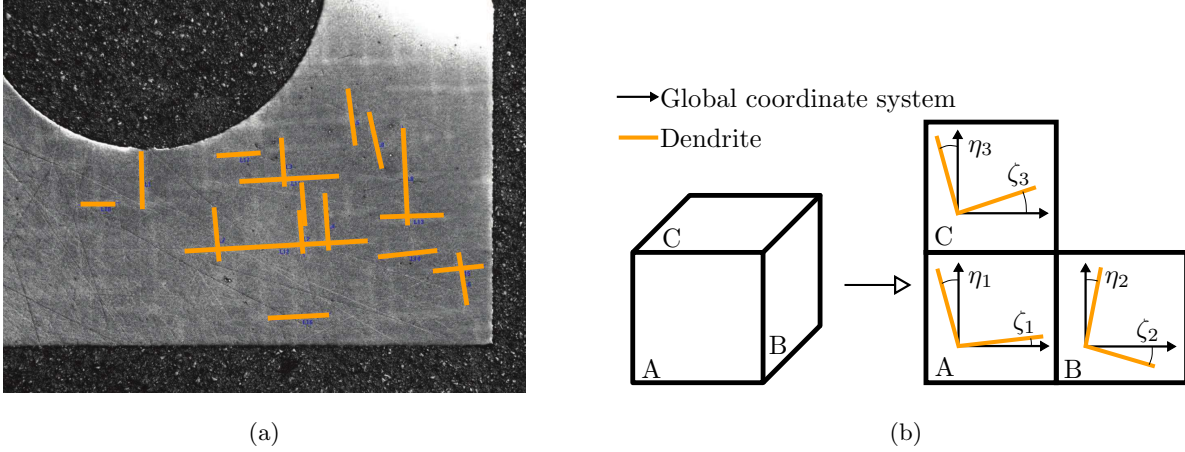


Figure 7: Depiction of the dendrites on one side of (a) the DCT1 specimen and (b) the studied surfaces for the measurement of the crystallographic orientation on the specimens.

These measurements of the dendrites contain a scatter, due to measurement inaccuracies and inhomogeneous crystallographic structures. In other words, not all measured angles for the visible dendrites are equal for the respective surface.

The scatter was accounted for by calculating the mean and standard deviation based on the 95% confidence interval. This means that for each surface in Fig. 7b a vertical and horizontal mean angle and associated maximum and minimum angles based on the 95% confidence interval were quantified. Hence, six angles for all surfaces were generated. It is to be noted that the crystallographic lattice vectors described by these angles are not intermutually orthogonal.

In the further FE-analyses, the crystallographic orientation needs to be described in terms of three orthogonal vectors. Thus, an optimisation procedure was carried out to ensure intermutual orthogonality. This was done by a Matlab [37] script with the objective to minimise the Root-Mean Square Errors (RMSE) of the six measured input angles relative to the corresponding angles of the vectors of the generated crystallographic orientation. This results in the best approximation of the crystallographic orientation based on the measured angles. An RMSE value of zero indicates that there is no discrepancy, whereas a high RMSE value indicates a large difference between them. The optimised crystallographic orientations in terms of sequential rotations about the global coordinate axes, as well as the RMSEs for the crystallographic orientations generated from the mean angles are shown in Table 5 for all specimens. The global coordinate axes are defined in both specimen geometries as follows: The z-axis corresponds to the casting direction; the x-axis to the negative Mode I crack growth direction and the y-axis is orthogonal to the previous two according to the right hand rule, *cf.* Fig. 2.

To account for the above mentioned scatter of the six measured angles, the same procedure was used to calculate a range of the crystallographic orientations. This was done by a series of optimisations using the above described routine, accounting for the confidence interval in the input of the angles.

Table 5: Optimised mean crystallographic orientation accounting for the misalignment in terms of sequential rotation about the global x-, y- and z-axis and the RMSEs.

Specimen	Kb1	Kb2	Kb3	Kb4	DCT1	DCT2	DCT3	DCT4
Rotation about x-axis [°]	1.7	-0.7	-1.4	6.3	-4.7	-3.7	-6.4	-2.0
Rotation about y-axis [°]	0.1	0.1	-2.3	-4.9	0.2	-3.6	-0.14	-3.2
Rotation about z-axis [°]	-2.8	-5.5	-5.8	-7.7	-5.4	-2.7	-19.9	-46.4
RMSE [°]	0.94	0.69	0.64	1.24	0.94	0.47	2.31	2.41

3. Resolved stress intensity factor parameters

In this section, a general framework for RSIFs acting on arbitrary material planes in anisotropic materials is defined. Hence, anisotropic SIFs are employed to describe the stress field around the crack tip and used in the two proposed crack driving force models to evaluate the RSIFs on arbitrary material planes. The anisotropic SIFs (K_I , K_{II} and K_{III}) can be evaluated in different ways. The approach in this work has been by using the Linear Elastic Fracture Mechanics (LEFM) M-Integral [38, 39] with incorporation of anisotropic material properties.

Based on the anisotropic SIFs, the stress field around the crack tip is calculated using the descriptions of the stresses near the crack tip in an anisotropic material developed by Hoenig [30]. This stress field expression is an extension of the work by Sih *et al.* [28], where the latter is only valid for the special case in which the plane of analysis is a plane of material symmetry. This would be the case for 2D-analyses (plane stress or plane strain). For cases where the plane of analysis is not a plane of material symmetry the work of Hoenig [30] has to be used. The use of a 3D-analysis enables the evaluation the RSIFs for every point along the crack front, which can suggest different active material planes through the thickness of the model. It is assumed that the most likely crack growth plane will depend on stresses very near the crack front, where one can assume a small region where there is no significant variation in the stress fields as one moves parallel to the crack front. Considering a local coordinate system

as depicted in Fig. 8a, the crack tip stresses developed in [30], in terms of the distance r and the angle θ , are defined as :

$$\begin{pmatrix} \sigma_{xx} \\ \sigma_{yy} \\ \sigma_{yz} \\ \sigma_{xz} \\ \sigma_{xy} \end{pmatrix} = \frac{1}{\sqrt{2\pi r}} \begin{pmatrix} Re \left(\sum_{i=1}^3 \frac{\mu_i^2 N_{ij}^{-1} K_j}{Q_i} \right) \\ Re \left(\sum_{i=1}^3 \frac{N_{ij}^{-1} K_j}{Q_i} \right) \\ -Re \left(\sum_{i=1}^3 \frac{\lambda_i N_{ij}^{-1} K_j}{Q_i} \right) \\ Re \left(\sum_{i=1}^3 \frac{\mu_i \lambda_i N_{ij}^{-1} K_j}{Q_i} \right) \\ -Re \left(\sum_{i=1}^3 \frac{\mu_i N_{ij}^{-1} K_j}{Q_i} \right) \end{pmatrix} = \frac{1}{\sqrt{2\pi r}} \begin{pmatrix} f_{xx}(K_I, K_{II}, K_{III}, \theta) \\ f_{yy}(K_I, K_{II}, K_{III}, \theta) \\ f_{yz}(K_I, K_{II}, K_{III}, \theta) \\ f_{xz}(K_I, K_{II}, K_{III}, \theta) \\ f_{xy}(K_I, K_{II}, K_{III}, \theta) \end{pmatrix} \quad (1)$$

$$\sigma_{zz} = -\frac{(S_{31}\sigma_{xx} + S_{32}\sigma_{yy} + S_{34}\sigma_{yz} + S_{35}\sigma_{zx} + S_{36}\sigma_{xy})}{S_{33}} = \frac{1}{\sqrt{2\pi r}} f_{zz}(K_I, K_{II}, K_{III}, \theta), \quad (2)$$

where K_j are the anisotropic SIFs, $Q_i = \sqrt{\cos \theta + \mu_i \sin \theta}$ and S is the material compliance matrix in Voigt notation using the following order for the stress and strain components as $[\sigma_{xx}, \sigma_{yy}, \sigma_{zz}, \sigma_{yz}, \sigma_{xz}, \sigma_{xy}]^T$ and $[\varepsilon_{xx}, \varepsilon_{yy}, \varepsilon_{zz}, 2\varepsilon_{yz}, 2\varepsilon_{xz}, 2\varepsilon_{xy}]^T$, see *e.g.* [40]. Furthermore, the quantities μ_i , λ_i and N_{ij} are derived from the material compliance matrix S , where it is to be noted that S is defined in the crack front coordinate system before extracting the quantities.

The parameters μ_i , $i = 1 \dots 3$, are the roots of the compatibility equation with positive imaginary parts, which are found from the characteristic sixth order polynomial equation [30]:

$$l_4(\mu)l_2(\mu) - l_3^2(\mu) = 0 \quad (3)$$

Solving Eq. 3 leads to three pairs of complex conjugate roots, where the ingoing

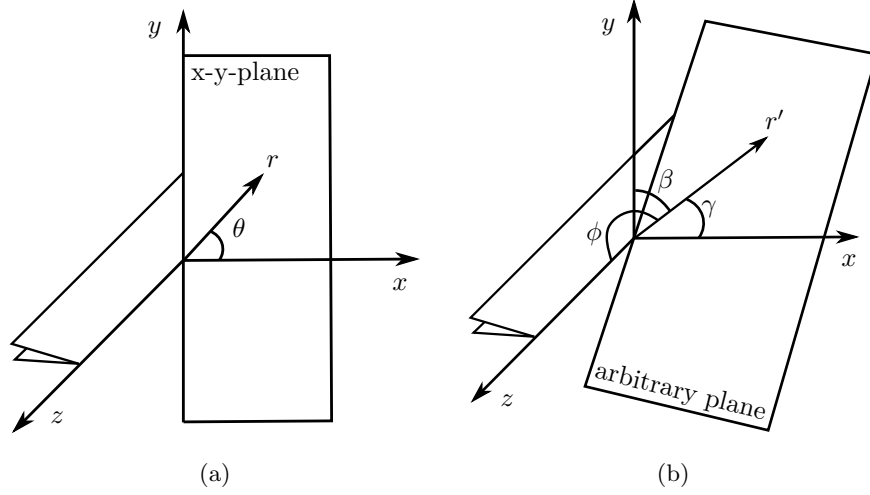


Figure 8: Illustration of the distance to the crack front (a) in terms of r on a plane orthogonal to the crack front and (b) in terms of r' on an arbitrary plane.

parameters are:

$$\begin{aligned}
 l_2(\mu) &= S'_{55}\mu^2 - 2S'_{45}\mu + S'_{44} \\
 l_3(\mu) &= S'_{15}\mu^3 - (S'_{14} + S'_{56})\mu^2 + (S'_{25} + S'_{46})\mu - S'_{24} \\
 l_4(\mu) &= S'_{11}\mu^4 - 2S'_{16}\mu^3 + (2S'_{12} + S'_{66})\mu^2 - 2S'_{26}\mu + S'_{22},
 \end{aligned} \tag{4}$$

where (for generalized plane deformation conditions)

$$S'_{pq} = S_{pq} - \frac{S_{p3}S_{3q}}{S_{33}}, \quad S'_{pq} \text{ is symmetric, } S'_{p3} = S'_{3p} = 0, \quad p, q = 1 \dots 6. \tag{5}$$

The parameter λ_i can be calculated by choosing the three positive imaginary parts of μ_i :

$$\lambda_i = -\frac{l_3(\mu_i)}{l_2(\mu_i)}, \quad i = 1 \dots 3 \tag{6}$$

and finally N_{ij} is defined as:

$$N_{ij} = \begin{bmatrix} 1 & 1 & 1 \\ -\mu_1 & -\mu_2 & -\mu_3 \\ -\lambda_1 & -\lambda_2 & -\lambda_3 \end{bmatrix} \tag{7}$$

For further details regarding these material functions see [30, 38, 39].

The stress tensor, when approaching the crack front along r , can now be defined by use of the stress components in Eqs. 1 and 2 accordingly:

$$\sigma_r(r, \theta) = \frac{1}{\sqrt{2\pi r}} \cdot \mathbf{f}(K_I, K_{II}, K_{III}, \theta), \quad (8)$$

where the subscript r denotes the direction along which the crack front is approached and the tensor \mathbf{f} is a function of the SIFs and θ . The anisotropic stress expression in Eq. 8, assumes implicitly that the crack front is approached along the direction defined by r and θ on the plane perpendicular to the crack front, according to Fig. 8a. Hence, r defines the distance from the crack front on the (perpendicular) x-y-plane. Extending the framework to arbitrary planes and directions, the distance from the crack front becomes r' , *cf.* Fig. 8b.

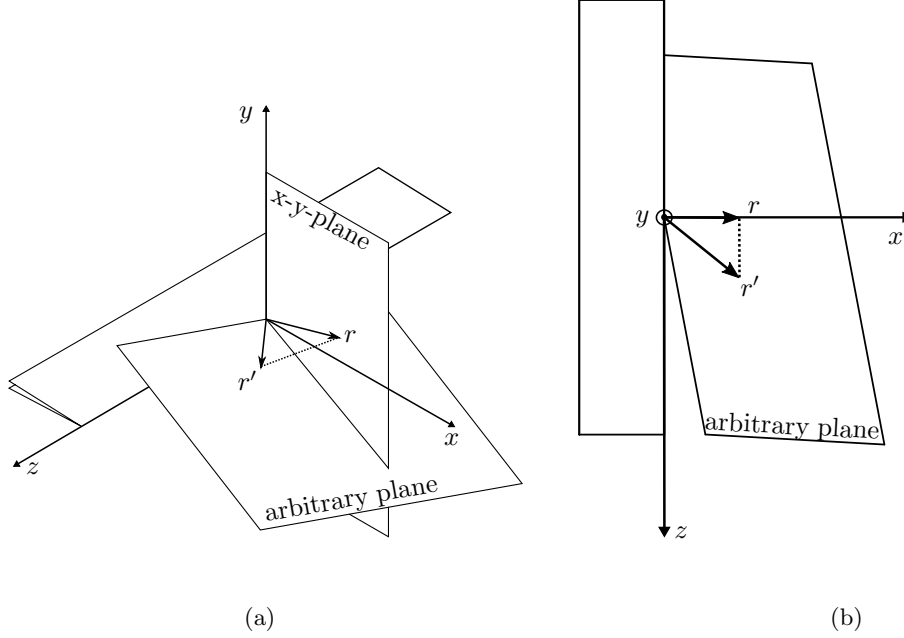


Figure 9: Illustration of the (a) projection of r' (lying on an arbitrary plane) onto the x-y-plane resulting in r and (b) from above viewing the x-z-plane.

Under the assumption that there are negligible variations in the stress field when moving a very short distance along the z -axis, the stress state at the distance r' can be determined by its projection onto the x-y-plane of the local

crack-front coordinate system as shown in Fig. 9. This results in a shorter distance r compared to r' to the crack front. In other words, the stresses will increase more slowly along r' than if the crack front is approached along the r direction, which implies that the SIF is scaled. Since SIFs are a measure of how the stresses increase as the crack front is approached the discrepancy between the lengths of r and r' has to be accounted for. This is done by the scaling factor $1/\sqrt{\cos^2 \gamma + \cos^2 \beta}$, that describes the geometrical relation of the lengths of r' and r , as $r' = r/\sqrt{\cos^2 \gamma + \cos^2 \beta}$, *cf.* Fig. 8, and consequently, $\theta = \arctan(\cos \beta / \cos \gamma)$. Using these relations and Eq. 8, the crack front can be thought to be approached along r' by incorporating the scaled tensor \mathbf{f}' , the stress state can be expressed by:

$$\begin{aligned} \sigma_{r'}(r, \gamma, \beta) &= \frac{(\cos^2 \gamma + \cos^2 \beta)^{0.25}}{\sqrt{2\pi r}} \cdot \mathbf{f}(K_I, K_{II}, K_{III}, \gamma, \beta) \\ &= \frac{1}{\sqrt{2\pi r}} \cdot \mathbf{f}'(K_I, K_{II}, K_{III}, \gamma, \beta). \end{aligned} \quad (9)$$

It should be pointed out that only the behaviour of the stresses is of interest as the distance from the crack front approaches zero and that no stresses along r' or r are to be evaluated. Based on this local stress state the RSIFs on an arbitrary plane in the material can now be defined.

Now, let \mathbf{n} be the unit normal vector of the arbitrary plane of interest, in which the unit vector \mathbf{s} (the direction of interest) lies. Note that $\gamma = \arccos(s_x)$, $\beta = \arccos(s_y)$ and $\phi = \arccos(s_z)$, where s_x , s_y and s_z are the x , y and z components of \mathbf{s} , *i.e.* $[s_x, s_y, s_z]^T$, meaning that the direction of \mathbf{s} coincides with r' . Furthermore, let $\mathbf{t} = \mathbf{s} \times \mathbf{n}$. By projecting the stress tensor (Eq. 9) on the plane and in the respective direction; \mathbf{n} , \mathbf{s} and \mathbf{t} and by multiplying with $\sqrt{2\pi r}$ the following local RSIF are defined:

$$\begin{aligned} k_I &= \mathbf{n} \cdot \mathbf{f}'(K_I, K_{II}, K_{III}, \gamma, \beta) \cdot \mathbf{n} \\ k_{II} &= \mathbf{s} \cdot \mathbf{f}'(K_I, K_{II}, K_{III}, \gamma, \beta) \cdot \mathbf{n} \\ k_{III} &= \mathbf{t} \cdot \mathbf{f}'(K_I, K_{II}, K_{III}, \gamma, \beta) \cdot \mathbf{n} \end{aligned} \quad (10)$$

The parameters k_I , k_{II} and k_{III} correspond to the three modes of fracture

resolved on a plane in a given direction \mathbf{s} , which from now on will be called the evaluation direction vector. Note that the RSIF parameters are denoted by a lower case k in order to distinguish them from the conventional SIF parameters K_I to K_{III} .

4. Crack driving force models

Adopting the the above defined general framework of RSIFs for the application of FCC single-crystal nickel-base superalloys, the arbitrary material planes are chosen to be the crystallographic slip planes. Two different crack driving force models have been evaluated and compared to the results from the performed experiments. The difference between the models lies in the choice of the evaluation direction \mathbf{s} , and its impact on the RSIF calculations, *cf.* Eq. 10. The evaluation directions will be chosen according to two different approaches, which are explained below. The evaluation planes are taken to be the $\{111\}$ crystallographic slip planes as they are potential locations for crack transitions from Mode I to crystallographic cracking as pointed out earlier. This means that k_I , k_{II} and k_{III} will be evaluated on the crystallographic slip planes, where k_I corresponds to the normal to the crystallographic slip plane, k_{II} to the evaluation direction vector \mathbf{s} and k_{III} to the direction \mathbf{t} perpendicular to both. Thus, the normal to the evaluation planes \mathbf{n} correspond in the proposed models to the normal to the crystallographic slip planes. It has earlier been proposed, in a 2D-context, that crystallographic cracking takes place on the slip plane, where the Mode II RSSIF is maximum [18]. In a 3D-context, this is assumed to corresponds to the maximum of $\sqrt{k_{II}^2 + k_{III}^2}$. Furthermore, it was proposed that not only the RSSIF (k_{II} , k_{III}), but also the resolved normal stress (by k_I) on the crystallographic slip plane contributes to crystallographic cracking. In order to account for this, an equivalent RSIF parameter k_{EQ} is proposed according to:

$$k_{EQ}(\mathbf{n}, \mathbf{s}) = \sqrt{\psi k_I^2 + k_{II}^2 + k_{III}^2}, \quad (11)$$

where ψ is a calibration parameter representing the contribution of k_I based on the observed cracking behaviour from the experiments. Further details of ψ

are given below. The formulation of this equivalent parameter k_{EQ} is based on the idea that the resolved shear stresses weaken the crystallographic plane by dislocation motion and that the resolved normal stress separates the surfaces [18], and thus both must be accounted for. This equivalent RSIF parameter will be evaluated in the two models, where the calibration parameter is set for each model to optimally predict the correct crystallographic cracking plane according to the experiments.

4.1. Model 1

This model is physically inspired by the micromechanisms occurring on the crystallographic level. The deformations in these materials are localised to the crystallographic slip planes in specific directions, and are associated to the dislocation motion [41]. Under loading, as the dislocation moves, the superpartial $\langle 101 \rangle$ will split up into two Shockley partials with the edge components $\langle 121 \rangle$. Thus, stresses in the primary $\langle 101 \rangle$ and secondary $\langle 121 \rangle$ crystallographic slip direction are of interest [5]. Furthermore, the normal stress to the crystallographic plane makes it easier or harder for slip to occur, and in turn for the crack to grow. In this model the evaluation direction \mathbf{s} corresponds to the primary crystallographic slip directions, *i.e.* Burgers' vectors \mathbf{b} , *cf.* Table 6, where all slip systems α , with the corresponding slip plane normal \mathbf{n}^α and slip direction \mathbf{b}^α are defined. For all three slip directions per plane also the negative direction vector is evaluated and the maximum value is chosen, *i.e.* $k_{EQ}(\mathbf{s} = \mathbf{b}) = \max\{k_{EQ}(\mathbf{b}), k_{EQ}(-\mathbf{b})\}$. This is due to the assumption that the sign of the physical slip direction is of no importance. Furthermore, it can be said that in this physically inspired model k_{II} corresponds to the primary and k_{III} to the secondary slip direction, where the latter is orthogonal to \mathbf{s} and \mathbf{n} , while k_I acts in the normal direction, which facilitates separation of the crack surfaces. An example of slip directions is shown in Fig. 10, where the three slip directions on the (111)-crystallographic slip plane are illustrated. It should be noted that the depicted coordinate system is the local crack front coordinate system, and not the material coordinate system in which the slip plane normal

Table 6: Definition of the slip systems α with corresponding slip plane normal \mathbf{n}^α and direction \mathbf{b}^α .

α	\mathbf{n}^α	\mathbf{b}^α
1	(111)	[01 $\bar{1}$]
2	(111)	$[\bar{1}01]$
3	(111)	[1 $\bar{1}0$]
4	($\bar{1}\bar{1}\bar{1}$)	[0 $\bar{1}1$]
5	($\bar{1}\bar{1}\bar{1}$)	$[\bar{1}0\bar{1}]$
6	($\bar{1}\bar{1}\bar{1}$)	[110]
7	($\bar{1}1\bar{1}$)	[011]
8	($\bar{1}\bar{1}1$)	[10 $\bar{1}$]
9	($\bar{1}1\bar{1}$)	$[\bar{1}\bar{1}0]$
10	($\bar{1}\bar{1}1$)	[0 $\bar{1}\bar{1}$]
11	($\bar{1}\bar{1}1$)	[101]
12	($\bar{1}\bar{1}1$)	$[\bar{1}10]$

direction and slip directions are defined.

4.2. Model 2

In this phenomenological model all possible evaluation directions \mathbf{s} on the crystallographic slip planes are considered and the direction with the corresponding maximum k_{EQ} is extracted. It is assumed that the resistance for transition to crystallographic crack growth is isotropic on the crystallographic planes in the sense that it is not a function of the evaluation direction \mathbf{s} . This is due to the assumption, that the shear stresses in an arbitrary direction on the crystallographic plane lead to shear motion in the same direction, resulting from an unspecified combination of dislocation motions on the atomic level and thus causing damage and finally crack growth. This means, that the model considers the direction in which the shear and normal stresses are maximum (k_I , k_{II} and k_{III}), and is not coupled to the physical micromechanisms of the single-crystal material in question. Thus, the slip plane which results in the highest k_{EQ} value will be deemed to be the crystallographic cracking plane. Therefore, k_{EQ} is com-

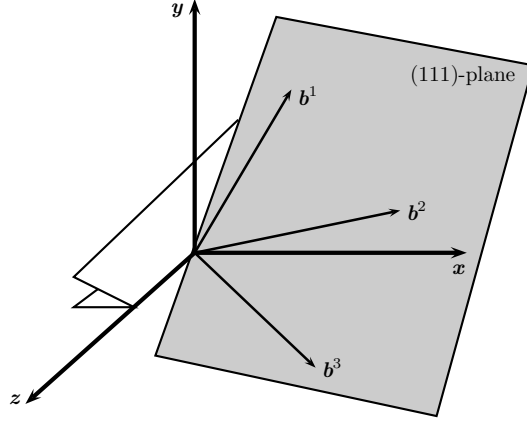


Figure 10: Evaluation directions for Model 1. Slip directions on the (111)-plane.

puted for all possible directions \mathbf{s} and the maximum is selected. It should be noted that all directions on the crystallographic plane are evaluated, *i.e.* in 360° about \mathbf{n} in steps of 1° , as illustrated in Fig. 11. Thus, $k_{EQ} = \max(k_{EQ}(\mathbf{s})), \forall \mathbf{s}$ on \mathbf{n} , where \mathbf{n} is the normal vector to the corresponding crystallographic slip plane.

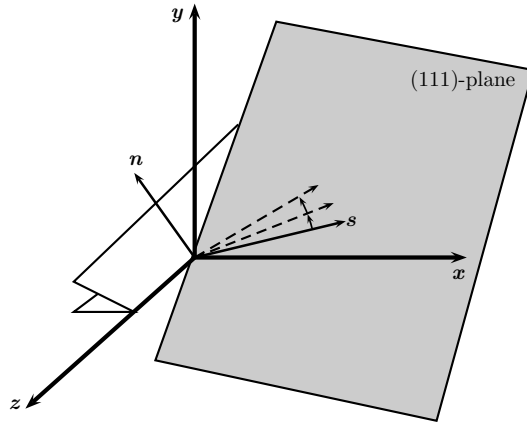


Figure 11: Evaluation directions on the (111)-plane for Model 2.

5. Simulations

Simulations for the two specimen geometries were performed in the FE-environment Abaqus V6.12 [42] and paired with the crack growth tool FRANC3D V7.0.8 [43]. All simulations were performed in a 3D-context. In order to handle the anisotropic constitutive behaviour an elastic anisotropic material description was used. The crystallographic orientation corresponding to the specimens in the experiments were accounted for in the material model, as discussed earlier. The two initial FE-models were each divided into a global and a local domain. A Mode I crack, representing the EDM notch in the specimen, was inserted in the local domain and then remeshed while the global domain retained its initial mesh. The two domains were then merged and analysed in the FE-solver. The resulting stress state was sent back to the crack evaluation tool, which calculated the anisotropic SIFs at each node along the crack front with the LEFM M-Integral technique [38, 39]. These anisotropic SIFs (K_I , K_{II} and K_{III}) are then used to calculate the RSIFs for each node along the crack front as described in Section 3.

Special care is taken in constructing the meshes in the crack front region, as illustrated in Fig. 12. The crack fronts are surrounded circumferentially by one ring of 15-noded wedge elements with appropriate nodes moved to quarter-point positions, and two rings of 20-noded brick elements. As shown in Fig. 12b, all near crack front elements have straight sides, effectively approximating the curved crack fronts with piecewise straight line segments. Using straight crack front segments eliminates the need to consider additional terms that arise in the M-integral if curvilinear element geometries are employed [44]. The domain of integration for the M-integral is the first two rings of elements, with the weighting function (virtual crack extension) being quadratic and centred on the element side nodes, as schematically shown in Fig. 12. This setup has previously been shown to produce accurate SIFs, see [39].

The Mode I cracks were automatically extended according to the magnitude of the anisotropic SIFs along the crack front. Since no crack growth law has

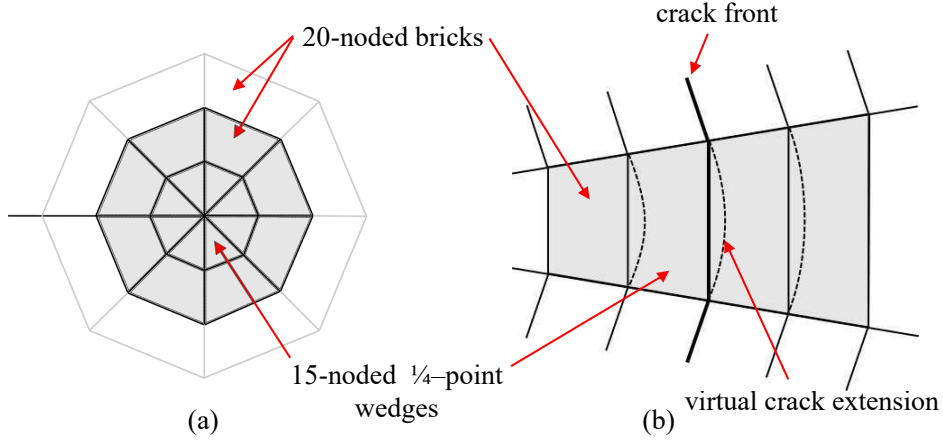


Figure 12: Meshing of the crack front, schematically showing (a) a cross-section with rings of eight 15- and 20-node elements placed circumferentially around the crack front, and (b) a plan view showing piecewise straight crack-front segments and virtual crack extensions used in the M-integral evaluation (right). The shaded area shows the domain of integration.

been used in this work, the quasi-static crack growth option in FRANC3D was used. This was done using a third-order polynomial fitting procedure for the SIF values along the crack front to approximate the shape of the next extended crack front. Hence, the crack fronts were extended stepwise, see [43] for further details. Using this procedure, the anisotropic SIFs along the crack front were evaluated for different crack lengths until the transition crack length was reached. The shape of the last Mode I crack fronts in the simulations were semi-elliptical (Kb) and a shallow semi-ellipse (DCT), based on the assumed experimental crack front shapes.

The above presented crystallographic crack driving force models were applied to the two specimen geometries and are evaluated below to identify the crystallographic cracking plane at the specific transition crack length determined experimentally. The evaluations were performed as a post-process treatment using Matlab 2017a [37]. Furthermore, since the experiments were isothermal, the temperature was assumed to be constant and homogeneous in the specimens, and thus a uniform expansion of the material does not induce any further stresses and can be neglected in the FE-models.

5.1. Kb model

The initial FE-model of the Kb specimen consisted of 6360 C3D20 brick and 16296 C3D10 tetrahedral elements. The whole model with the remeshed local domain (inclusion of the initial crack) consists of 6104 C3D20 hexahedral, 40880 C3D10 tetrahedral and 340 C3D15 wedge elements. The elements are standard ABAQUS elements and are labelled accordingly [42]. The FE-model can be seen in Fig. 13, where the local domain is highlighted in the center of the model.

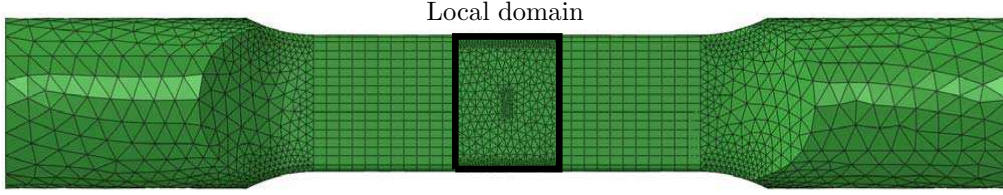


Figure 13: FE-model of the Kb specimen.

The following boundary conditions were applied; a fixed support at the left surface and a concentrated force to one master node on the right surface. This force corresponds to the one in the respective experiment. The master node was coupled to all other nodes of the surface by a constraint that restrained motion in the plane and gave an equal deformation in the axial direction. An initial semi-circular Mode I crack with a radius of 0.5 mm was inserted and then extended stepwise through the mesh, as described above, until the transition crack length was reached, *cf.* Table 4.

5.2. DCT model

The initial DCT FE-model consisted of 23840 C3D20 brick elements. The remeshed model consisted of 20500 C3D20 brick, 25700 C3D10 tetrahedral and 300 C3D15 wedge elements. The FE-model can be seen in Fig. 14, where the local domain is highlighted in the center of the model. The boundary conditions were; a coupling constraint of the translational and rotational motion of the surfaces in the pin holes relative to a reference point located in the center of

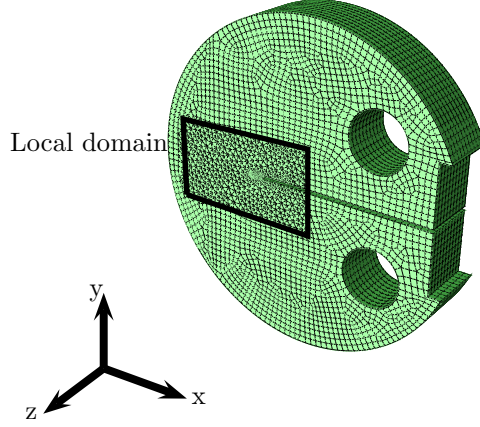


Figure 14: FE-model of the DCT specimen.

each pin hole; translation of the reference point in the bottom pin hole was restricted in all directions but the z-direction, and only the rotation around the z-axis was free. The reference point in the top pin hole was only allowed to move in the y- and z-direction, and all rotations but the rotation about the z-axis were restrained. The loading force was applied to this reference node in the positive y-direction. Furthermore, one point at the edge of each pin hole was fixed in the z-direction. An initial straight Mode I through-crack with a length of 0.5 mm, measured from the notch, was inserted and then extended stepwise through the model until the transition crack length was reached, *cf.* Table 4. It may be noted, that as the crack is extended it changes its shape to become part of a semi-ellipse, which is very shallow.

6. Predictions and discussion

In this section the above described equivalent RSIF parameter k_{EQ} is evaluated according to the two presented models. As explained in Subsection 2.4, the scatter due to the measurements of the dendrites was accounted for by the computed ranges of the possible crystallographic orientations. These, in turn, gave a scatter band for the calculated k_{EQ} parameter values, from which one

crystallographic orientation corresponds to the mean of the measured angles, and the others correspond to the scatter based on standard deviation in the 95% confidence interval. The lower boundary of the scatter band was determined by the crystallographic orientation that results in the lowest sum of k_{EQ} values summed over all nodes along the crack front. Equally so for the upper boundary with its highest total k_{EQ} parameter value. These need not necessarily correspond to the minimum and maximum angles in the confidence interval of the measured dendrites. This procedure is based on the fact, that the change of crystallographic orientation has the same effect on the k_{EQ} values for all nodes along the crack front, and results thus only in an up- or downwards shift of the k_{EQ} -curve.

The value of the calibration parameter ψ , *cf.* Eq. 11, was chosen to fit the experimental results from the DCT specimens based on the FE-simulations of the DCT model. This was done by an iterative fitting of the calculated RSIF parameters in relation to the observed experimental crystallographic cracking planes. The same calibration parameter was then used in the prediction of the crystallographic cracking plane in the Kb specimens. Fitting to the DCT specimens was done due to fewer specimens with crystallographic crack growth compared to the Kb specimens. The values were determined to be $\psi = 0.1$ for Model 1 and $\psi = 0.2$ for Model 2.

Incorporating the scatter in the two models, the k_{EQ} parameter values were evaluated for all specimens and are displayed in Table 7. For Model 1 it can be seen that only the slip direction with the highest k_{EQ} value on each of the slip planes is presented for each side of the crack. For Model 2 the k_{EQ} value is presented for all slip planes on each side of the crack. The presented values for the left (L) and right (R) side of the specimens were evaluated at a normalised crack front distance of 0.05 and 0.95, respectively, *cf.* Fig. 15. This is done to avoid numerical errors that occur due to a change of order of the singularity when the crack approaches a free surface of the FE-model. The generalized plane deformation condition is assumed to hold all the way to the free surface when computing the anisotropic SIFs, even though this is not true.

More importantly, it is difficult to generate well shaped elements at the crack front near a free surface, and the local errors due to elements that are poorly shaped and not symmetrical about the crack front lead to errors. Furthermore, it could be observed from the experimental results that the location of the cracking mode transition occurred at the surface of the specimen. Hence, the results from the FE-simulations were extracted and evaluated here (at 0.05 and 0.95 along the normalised crack front distance). The evaluated crack lengths in the FE-simulations correspond to the experimentally found crack lengths for the transition from Mode I to crystallographic cracking.

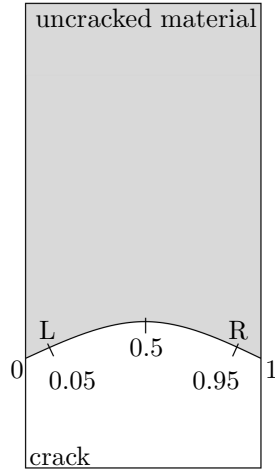


Figure 15: Illustration of the normalised distance along the crack front for a DCT specimen.

Table 7: Summary of the k_{EQ} parameter results. The three presented values are; lower limit of the scatter band < mean value < upper limit of the scatter band. The grey highlighted results represent the active slip plane observed in the experiments and the number in parenthesis for Model 1 represents the slip system α as shown in Table 6. Units in [MPa $\sqrt{\text{m}}$].

		Side	k_{EQ} on (111)-plane	k_{EQ} on ($\bar{1}\bar{1}\bar{1}$)-plane	k_{EQ} on ($\bar{1}\bar{1}\bar{1}$)-plane	k_{EQ} on ($\bar{1}\bar{1}\bar{1}$)-plane
Kb1	Model 1	L	7.95 < 8.35 < 8.60 (3)	6.31 < 6.98 < 7.59 (5)	8.20 < 8.65 < 8.90 (9)	6.97 < 7.64 < 8.18 (11)
		R	7.45 < 8.05 < 8.48 (2)	8.05 < 8.40 < 8.75 (6)	6.04 < 6.72 < 7.40 (8)	8.20 < 8.55 < 8.85 (12)
	Model 2	L	9.25 < 9.65 < 9.9	7.62 < 7.97 < 8.21	9.70 < 10.02 < 10.25	8.32 < 8.51 < 8.76
		R	8.84 < 9.11 < 9.31	9.60 < 9.95 < 10.15	7.14 < 7.53 < 7.72	9.43 < 9.82 < 10.10
Kb2	Model 1	L	2.90 < 3.15 < 3.36 (1)	2.81 < 2.92 < 3.03 (5)	3.24 < 3.44 < 3.57 (7)	2.86 < 2.93 < 3.04 (11)
		R	2.78 < 2.88 < 2.98 (2)	3.23 < 3.44 < 3.58 (4)	2.83 < 2.94 < 3.04 (8)	2.90 < 3.10 < 3.31 (10)
	Model 2	L	3.87 < 3.93 < 4.15	2.95 < 3.06 < 3.19	4.05 < 4.18 < 4.32	3.11 < 3.28 < 3.43
		R	3.12 < 3.24 < 3.40	3.67 < 3.85 < 4.13	2.89 < 3.06 < 3.21	4.04 < 4.19 < 4.35
Kb3	Model 1	L	1.93 < 2.04 < 2.13 (1)	1.76 < 1.91 < 2.06 (5)	2.14 < 2.24 < 2.31 (7)	1.86 < 1.97 < 2.11 (11)
		R	1.72 < 1.79 < 1.94 (2)	2.13 < 2.25 < 2.33 (4)	1.77 < 1.92 < 2.43 (8)	1.90 < 2.03 < 2.13 (10)
	Model 2	L	2.34 < 2.58 < 2.71	1.91 < 2.05 < 2.19	2.56 < 2.74 < 2.91	2.13 < 2.28 < 2.44
		R	1.98 < 2.11 < 2.27	2.53 < 2.72 < 2.85	1.95 < 2.07 < 2.20	2.33 < 2.48 < 2.62
Kb4	Model 1	L	5.81 < 6.21 < 6.54 (3)	5.18 < 5.22 < 5.32 (6)	6.43 < 6.77 < 7.06 (9)	6.47 < 6.90 < 7.27 (11)
		R	6.14 < 6.59 < 6.85 (2)	6.31 < 6.37 < 6.59 (6)	4.40 < 4.91 < 5.45 (9)	6.76 < 7.14 < 7.30 (12)
	Model 2	L	7.31 < 7.62 < 7.94	5.70 < 5.98 < 6.22	7.51 < 7.89 < 8.21	7.30 < 7.59 < 7.71
		R	7.19 < 7.51 < 7.81	7.59 < 7.93 < 8.29	5.31 < 5.58 < 5.84	7.54 < 8.06 < 8.34
DCT1	Model 1	L	11.65 < 12.45 < 13.40 (3)	13.03 < 13.49 < 13.84 (4)	12.42 < 12.95 < 13.45 (7)	12.39 < 13.02 < 13.78 (10)
		R	11.70 < 12.33 < 12.87 (3)	11.98 < 12.52 < 12.91 (4)	13.15 < 13.78 < 14.3 (7)	11.07 < 11.75 < 12.42 (10)
	Model 2	L	14.59 < 14.92 < 15.31	14.56 < 14.88 < 15.21	14.29 < 14.66 < 15.01	13.78 < 14.24 < 14.60
		R	13.65 < 14.16 < 14.42	14.48 < 14.85 < 15.27	15.45 < 15.75 < 16.11	13.66 < 13.92 < 14.54
DCT2	Model 1	L	14.79 < 15.15 < 15.49 (1)	15.94 < 16.27 < 16.64 (4)	14.70 < 15.08 < 15.42 (7)	15.94 < 16.42 < 16.82 (10)
		R	15.6 < 16.10 < 16.37 (1)	14.42 < 14.44 < 14.71 (4)	16.83 < 17.30 < 17.6 (7)	14.32 < 14.34 < 14.4 (10)
	Model 2	L	17.45 < 17.91 < 18.37	17.43 < 17.75 < 18.06	17.31 < 17.78 < 18.11	17.51 < 17.98 < 18.48
		R	17.02 < 17.41 < 17.75	17.65 < 18.00 < 18.21	18.31 < 18.78 < 19.24	17.84 < 18.08 < 18.43
DCT3	Model 1	L	8.90 < 9.10 < 9.44 (3)	9.74 < 10.13 < 10.20 (4)	8.67 < 9.02 < 9.36 (7)	8.42 < 9.22 < 9.85 (10)
		R	7.09 < 8.27 < 9.08 (3)	8.84 < 9.23 < 9.45 (4)	10.3 < 10.61 < 10.81 (7)	8.04 < 8.65 < 9.20 (12)
	Model 2	L	10.65 < 10.91 < 11.27	10.63 < 11.06 < 11.52	10.01 < 10.30 < 10.52	9.51 < 9.96 < 10.27
		R	6.39 < 6.88 < 7.41	10.02 < 10.29 < 10.53	11.34 < 11.87 < 12.21	9.69 < 9.97 < 10.40
DCT4*	Model 1	L	12.03 < 12.53 < 13.29 (3)	13.23 < 14.02 < 14.61 (4)	12.56 < 13.77 < 14.57 (8)	8.42 < 9.20 < 10.88 (12)
		R	9.28 < 9.97 < 11.46 (3)	13.67 < 14.64 < 15.14 (5)	11.53 < 12.82 < 13.85 (7)	12.33 < 12.46 < 12.95 (12)
	Model 2	L	13.47 < 14.14 < 14.76	16.35 < 17.10 < 17.69	16.31 < 17.15 < 17.83	9.81 < 10.30 < 10.99
		R	10.10 < 10.66 < 11.28	16.85 < 17.39 < 18.11	15.94 < 16.59 < 17.10	13.60 < 14.22 < 14.81

* no crystallographic crack growth in DCT4. k_{EQ} evaluated at crack length of 2.4 mm

As the transition crack lengths were different in each of the specimens, and also the lengths of the crack fronts, a direct comparison between the specimens could not be performed with the normalised crack front lengths. To determine if the correct crystallographic cracking plane is predicted with the proposed crystallographic crack growth parameter, the crystallographic planes with the highest k_{EQ} values at each side of the specimens are to coincide with the crystallographic cracking planes in the experiments. Thus, when evaluating k_{EQ} it can be seen that this is possible. For instance, from the simulations of the Kb1 specimen, it can be seen in Table 7 that on the left side the $(\bar{1}\bar{1}\bar{1})$ -plane and on the right side the $(\bar{1}\bar{1}1)$ -plane experience the highest stress intensities in terms of k_{EQ} . This can be validated by the experiments which show that the global crystallographic crack started to grow on these two planes on the corresponding sides, *cf.* Table 4. The crystallographic crack initiates first on the $(\bar{1}\bar{1}\bar{1})$ -plane at a crack length of 0.95 mm and then at 1 mm on the $(\bar{1}\bar{1}1)$ -plane, where a slightly higher k_{EQ} value for the $(\bar{1}\bar{1}\bar{1})$ -plane than for the $(\bar{1}\bar{1}1)$ -plane is obtained in the evaluations, see Table 7. This means that at the crack length of 0.95 mm the transition to the $(\bar{1}\bar{1}\bar{1})$ -plane occurs on the left side before the crack transition to the $(\bar{1}\bar{1}1)$ -plane on the right side. Employing the same argument in the other simulations, it can be stated that the correct crystallographic plane on which crystallographic crack growth first occurs is predicted in all investigated cases using the k_{EQ} parameter. A summary is given in Table 8, where it can be concluded from the values of the calibration parameter that the resolved shear stresses (k_{II} and k_{III}) as well as the normal stress (k_I) to the crystallographic slip plane are of importance.

It should be noted, that the models are only able to predict the first occurrence of transition to crystallographic crack growth. This is due to a redistribution of the stress state when the crack transitions to a crystallographic crack on one side of the specimen, since this changes the crack geometry and the stress state. Thus, the presented framework is only valid for the prediction of the crystallographic cracking plane of the first transition from Mode I to crystallographic cracking or when the transition occurs almost simultaneously, *i.e.* the

stress state and crack shape do not change to any greater extent.

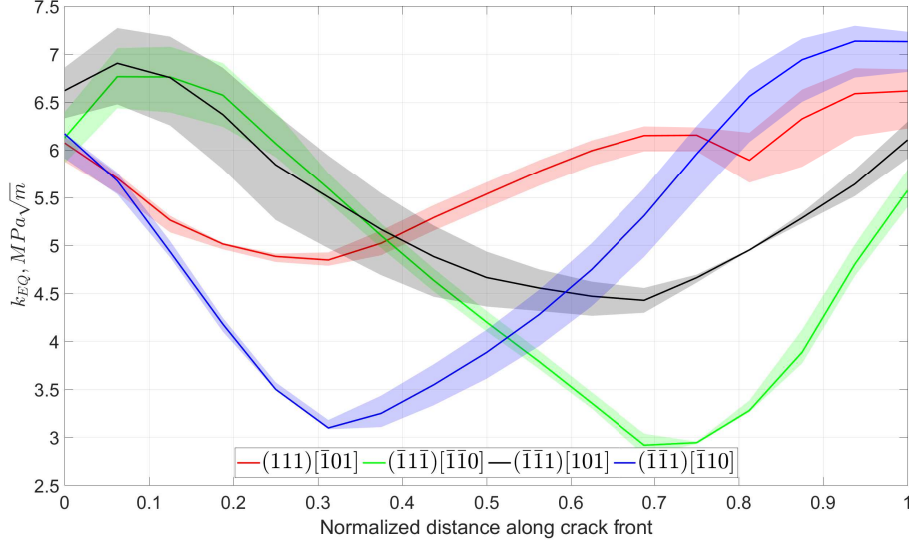


Figure 16: The k_{EQ} parameter evaluated by Model 1 as a function of normalised crack growth distance for two slip systems giving the highest values on each side of the model for Kb4 at the transition crack length 1 mm with the corresponding crack depth of 0.9 mm.

For Kb4 and DCT3, Model 1 predicts the correct crystallographic cracking plane only when accounting for the scatter in the crystallographic orientations. The uncertainties about the crystallographic orientation is especially high in these two specimens, see the higher RMSE-values in Table 5. Thus, it is reasonable to account for the scatter in these cases. This is exemplified in Fig. 16, where the k_{EQ} parameter is presented as a function of the normalised distance along the crack front for Kb4. It can be seen that only by including the scatter bands, which are depicted as shady surfaces, the experimentally observed crystallographic cracking plane could be predicted. The curves oscillate because of the geometrical intersections of the crack front coordinate system with the evaluation directions, which is defined in the material coordinate system. Thus, a higher curvature of the crack front results in more oscillation of the resulting k_{EQ} -curves. Model 2 shows a good capability to predict the correct crystal-

lographic cracking planes, and when employing the scatter for Kb2, Kb4 and DCT3, it could predict the correct crystallographic slip planes in all specimens.

The importance of the crystallographic orientation can directly be seen in the k_{EQ} magnitudes of the scatter bands in Table 7. Depending on the standard deviations for the measured angles the scatter bands are smaller or bigger, and can have a major influence on the results. This shows the importance of the material orientation when computing the RSIF parameters.

In the DCT4 specimen no crystallographic crack growth occurred. This can be explained by the physical location of the crystallographic plane experiencing the highest k_{EQ} value, which is the $(1\bar{1}\bar{1})$ -plane. As depicted in Fig. 6 the intersection of the $(1\bar{1}\bar{1})$ -plane with the fracture surface lies parallel with crack growth direction. This makes it unlikely for the crack to transition and grow on the $(1\bar{1}\bar{1})$ -plane, or any other octahedral plane due to the crystallographic orientation present in this specimen. Thus, Mode I crack growth is dominant throughout the whole specimen. Again, this points towards the effect and importance of the orientation of the crystallographic structure in these materials.

Table 8: Summary of the k_{EQ} parameter predicting cracking planes compared to the experiments.

	ψ	Kb1	Kb2	Kb3	Kb4	DCT1	DCT2	DCT3	DCT4
Model 1	0.1	yes	yes	yes	yes*	yes	yes	yes*	-**
Model 2	0.2	yes	yes*	yes	yes*	yes	yes	yes*	-**

*within error margin

**no crystallographic crack growth

It should be stated that the execution time of Model 2 is substantially higher than the one of Model 1, since a lot more directions have to be evaluated.

Furthermore, the comparison of the angle between the evaluation direction in Model 2, which gave the highest k_{EQ} value (red direction vector), and the Burgers' direction (positive and negative) in Model 1 (black direction vectors) is schematically depicted in Fig. 17. The inserted symbols represent the angular

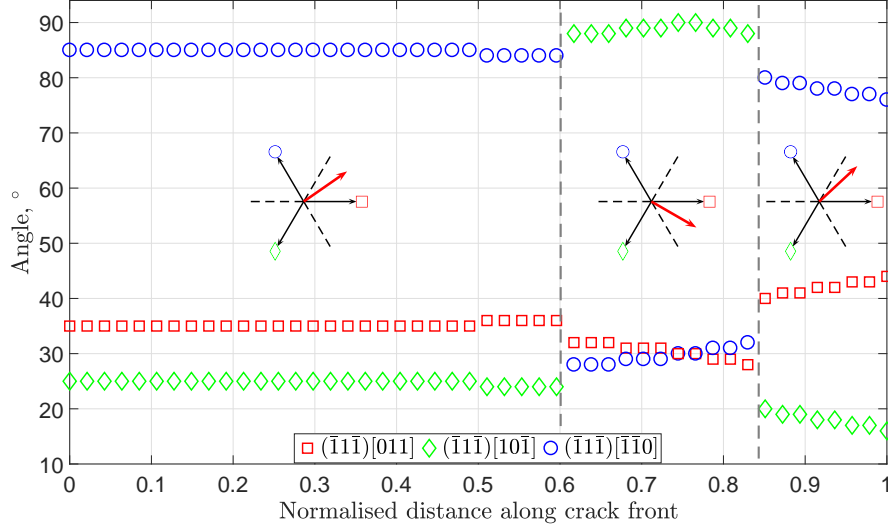


Figure 17: Angle between maximum k_{EQ} (red direction vector) in Model 2 and the three Burgers' vectors on the $(\bar{1}\bar{1}\bar{1})$ -plane along the normalised crack front for DCT1 at the transition crack length 2.6 mm.

difference between the above mentioned direction in Model 2 and the three Burgers' directions on the active crystallographic cracking plane $(\bar{1}\bar{1}\bar{1})$ according to Model 1 for the DCT1 specimen. It can be seen that in an interval between 0.61 and 0.83 of the normalised crack front, the evaluation direction, which gave the highest k_{EQ} value in Model 2, switches direction and thus the angles to the Burgers' vector change. Apart from the mentioned interval, it can be noted that the depicted angles as a function of normalised distance along the crack front are continuous with a continuous first derivative and are almost constant. The minimum angle is in the interval of 16° - 30° , meaning that the maximum k_{EQ} -direction will never coincide with the favoured slip directions (Burgers' directions) with the least material resistance to slip, as in Model 1. This was to be expected, since the Burger's directions possess predefined directions solely depending on the physical orientation of the crystal with respect to the specimen

geometry, whereas the highlighted directions determined by Model 2 depend on the local stress state and the above described calibration parameter.

This study focuses on the prediction of the active crystallographic cracking planes from a crack front perpendicular to the loading direction. However, the results suggest that Model 1 and 2, with the proposed RSIF parameter k_{EQ} , are promising candidates to also serve as a foundation for quantifying the transition between Mode I and crystallographic cracking and to predict the crystallographic crack growth behaviour.

Some difficulties should be noted while evaluating the presented RSIF parameter. One difficulty lies in the evaluation of the crystallographic misalignments of the specimens, which are measured from the dendrites' projections on the surface of the specimens, where measuring inaccuracies can cause errors. It should be kept in mind that this issue will also occur in real applications where it is often difficult to determine the secondary crystallographic orientation. Furthermore, the crack front shape before transition from Mode I to crystallographic cracking was only idealised and assumed to be semi-circular and semi-elliptical, respectively. The actual crack front shape can deviate from this and therefore change the stress field around the crack tip, thus influencing the results.

Finally, it can be stated that more work is needed before the presented method is applicable in an industrial context. Work has been initiated to automate the procedure for a more applicable usage. Furthermore, more experiments and also real component geometries should be evaluated to validate the method further. The authors believe that the procedure can be adapted to high temperature applications yielding nonlinear effects, with some modifications. Inelastic effects can, for instance, be incorporated by a procedure similar to the one described in Busse *et al.* [45].

7. Conclusions

From the presented results the following can be concluded:

1. The developed crystallographic crack driving force parameter k_{EQ} can successfully predict the active crystallographic cracking plane at the transition from a Mode I crack.
2. The crystallographic orientation of the material with respect to the geometry is of major importance when computing the crystallographic crack driving force parameters.
3. Model 1 and 2 are promising candidates for predicting the crystallographic crack propagation rate and when the transition of cracking modes occurs.

Acknowledgements

This research has been funded by the Swedish Energy Agency and Siemens Industrial Turbomachinery AB through the Research Consortium of Materials Technology for Thermal Energy Processes, Grant no. KME-702, the support of which is gratefully acknowledged. The authors would also like to thank Dr. Paul Wawrzynek at Fracture Analysis Consultants Inc. for valuable discussions and support and Johanna Simonsson at Siemens Industrial Turbomachinery AB for her laboratory work.

References

- [1] International Energy Agency, World Energy Outlook 2015, OECD/IEA, 2015.
- [2] R. Reed, The Superalloys-Fundamentals and Applications, Cambridge University Press, Cambridge, UK, 2006.
- [3] A. Pineau, S. D. Antolovich, High temperature fatigue of nickel-base superalloys - A review with special emphasis on deformation modes and oxidation, Engineering Failure Analysis 16 (2009) 2668–2697.
- [4] D. Leidermark, J. Moverare, K. Simonsson, S. Sjöström, S. Johansson, Room temperature yield behaviour of a single-crystal nickel-base superalloy

- with tension/compression asymmetry, *Computational Materials Science* 47 (2009) 366–372.
- [5] D. P. Pope, S. S. Ezz, Mechanical properties of Ni3Al and nickel-base alloys with high volume fraction of gamma prime, *International metals reviews* 29 (1984) 136–167.
 - [6] M. Segersäll, J. Moverare, D. Leidermark, K. Simonsson, Low-cycle fatigue behaviour of a Ni-based single-crystal superalloy, volume 891-892, 2014. doi:10.4028/www.scientific.net/AMR.891-892.416.
 - [7] R. Naik, D. DeLuca, D. Shah, Critical plane fatigue modeling and characterization of single crystal nickel superalloys, *Journal of Engineering for Gas Turbines and Power* 126 (2004).
 - [8] D. Leidermark, M. Segersäll, Modelling of thermomechanical fatigue stress relaxation in a single-crystal nickel-base superalloy, *Computational Materials Science* 90 (2014) 61–70.
 - [9] R. L. Amaro, S. D. Antolovich, R. W. Neu, A. Staroselsky, Physics-Based Modeling of Thermo-Mechanical Fatigue in PWA 1484, in: *Superalloys 2012*, 2012, pp. 481–490. doi:10.1002/9781118516430.ch53.
 - [10] J. Moverare, R. Reed, Thermomechanical fatigue in single crystal superalloys, in: *MATEC Web of Conferences*, volume 14, 2014. doi:10.1051/mateconf/20141406001.
 - [11] M. Segersäll, J. J. Moverare, D. Leidermark, K. Simonsson, Creep and stress relaxation anisotropy of a single-crystal superalloy, in: *Metallurgical and Materials Transactions A: Physical Metallurgy and Materials Science*, volume 45, 2014, pp. 2532–2544. doi:10.1007/s11661-014-2198-0.
 - [12] J.-B. Le Graverend, J. Cormier, F. Gallerneau, P. Villechaise, S. Kruch, J. Mendez, A microstructure-sensitive constitutive modeling of the inelastic behavior of single crystal nickel-based superalloys at very high temperature, *International Journal of Plasticity* 59 (2014).

- [13] D. Leidermark, J. Moverare, K. Simonsson, S. Sjöström, A combined critical plane and critical distance approach for predicting fatigue crack initiation in notched single-crystal superalloy components, *International Journal of Fatigue* 33 (2011) 1351–1359.
- [14] B. F. Antolovich, A. Saxena, S. D. Antolovich, Fatigue crack propagation in single-crystal CMSX- 2 at elevated temperature, *Journal of Materials Engineering and Performance* 2 (1993) 489–495.
- [15] T. Tinga, Stress intensity factors and crack propagation in a single crystal nickel-based superalloy, *Engineering Fracture Mechanics* 73 (2006) 1679–1692.
- [16] H. Kagawa, Y. Mukai, The Effect of Crystal Orientation and Temperature on Fatigue Crack Growth of Ni-Based Single Crystal Superalloy, *John Wiley and Sons*, 2012, pp. 225–233. doi:10.1002/9781118516430.ch25.
- [17] K. S. Chan, J. Feiger, Y. D. Lee, R. John, S. J. Hudak, Fatigue crack growth thresholds of deflected mixed-mode cracks in PWA1484, volume 127, 2005, pp. 2–7. doi:10.1115/1.1836765.
- [18] J. Telesman, L. J. Ghosn, Fatigue crack growth behavior of PWA 1484 single crystal superalloy at elevated temperatures, *Journal of Engineering for Gas Turbines and Power* 118 (1996) 399–405.
- [19] D. MacLachlan, D. Knowles, Fatigue behaviour and lifing of two single crystal superalloys, *Fatigue and Fracture of Engineering Materials and Structures* 24 (2001).
- [20] N. Hou, W. Gou, Z. Wen, Z. Yue, The influence of crystal orientations on fatigue life of single crystal cooled turbine blade, *Materials Science and Engineering: A* 492 (2008) 413–418.
- [21] C. Busse, J. Homs, D. Gustafsson, F. Palmert, B. Sjödin, J. Moverare, K. Simonsson, D. Leidermark, A finite element study of the effect of crystal

- orientation and misalignment on the crack driving force in a single-crystal superalloy, in: *Proceedings of the ASME Turbo Expo*, volume 7A-2016, 2016. doi:10.1115/GT2016-56305.
- [22] M. Segersäll, D. Leidermark, J. J. Moverare, Influence of crystal orientation on the thermomechanical fatigue behaviour in a single-crystal superalloy, *Materials Science and Engineering A* 623 (2015) 68–77.
 - [23] H. W. Liu, Q. Chen, D. Lai, Shear fatigue crack growth and its analysis 29 (1993) 300–307.
 - [24] Q. Chen, H. Liu, Resolved shear stress intensity coefficient and fatigue crack growth in large crystals, *Theoretical and Applied Fracture Mechanics* 10 (1988) 111–122.
 - [25] M. Gell, G. Leverant, The characteristics of stage I fatigue fracture in a highstrength nickel alloy, *Acta Metallurgica* 16 (1968) 553–561.
 - [26] S. Ranjan, N. K. Arakere, A Fracture-Mechanics-Based Methodology for Fatigue Life Prediction of Single Crystal Nickel-Based Superalloys, *Journal of Engineering for Gas Turbines and Power* 130 (2008) 032501.
 - [27] W. Qiu, X. Ma, S. Rui, H.-J. Shi, Crystallographic analysis on small fatigue crack propagation behaviour of a nickel-based single crystal superalloy, *Fatigue and Fracture of Engineering Materials and Structures* 40 (2017).
 - [28] G. C. Sih, P. C. Paris, G. R. Irwin, On cracks in rectilinearly anisotropic bodies, *International Journal of Fracture Mechanics* 1 (1965) 189–203.
 - [29] P. A. Sabnis, S. Forest, J. Cormier, Microdamage modelling of crack initiation and propagation in FCC single crystals under complex loading conditions, *Computer Methods in Applied Mechanics and Engineering* 312 (2016) 468–491.
 - [30] A. Hoenig, Near-tip behavior of a crack in a plane anisotropic elastic body, *Engineering Fracture Mechanics* 16 (1982) 393–403.

- [31] R. Reed, J. Moverare, A. Sato, F. Karlsson, M. Hasselqvist, A New Single Crystal Superalloy for Power Generation Applications, *Superalloys 2012* (2012) 197–204.
- [32] A. Coles, R. E. Johnson, H. G. Popp, Utility of surface-flawed tensile bars in cyclic life studies, *Journal of Engineering Materials and Technology, Transactions of the ASME* 98 (1976) 305–315.
- [33] F. Palmert, J. Moverare, D. Gustafsson, C. Busse, Fatigue crack growth behaviour of an alternative single crystal nickel base superalloy, *International Journal of Fatigue* 109 (2018) 166–181.
- [34] ASTM, Test Method for Measurement of Fatigue Crack Growth Rates, Technical Report, 2012. doi:10.1520/e0647-12.
- [35] K. Schwalbe, D. Hellmann, Application of the Electrical Potential Method to Crack Length Measurements using Johnson’s Formula, *Journal of Testing and Evaluation* 9 (1981) 218–221.
- [36] J. Telesman, L. J. Ghosn, The unusual near-threshold FCG behavior of a single crystal superalloy and the resolved shear stress as the crack driving force, *Engineering Fracture Mechanics* 34 (1989) 1183–1196.
- [37] Mathworks, Matlab 2014b, 2000.
- [38] P. A. Wawrzynek, B. J. Carter, L. Banks-Sills, The M-integral for computing stress intensity factors in generally anisotropic materials, NASA, Marshall Space Flight Center, Huntsville, USA, 2005.
- [39] L. Banks-Sills, P. A. Wawrzynek, B. Carter, A. R. Ingraffea, I. Hershkowitz, Methods for calculating stress intensity factors in anisotropic materials: Part II-Arbitrary geometry, *Engineering Fracture Mechanics* 74 (2007) 1293–1307.
- [40] T. C. T. Ting, *Anisotropic Elasticity : Theory and Applications*, Oxford University Press, New York, NY, USA, 1996.

- [41] D. R. Askeland, P. P. Phule, The Science and Engineering of Materials, fifth edit ed., Thomson, Canada, Toronto, 2006.
- [42] ABAQUS, ABAQUS 6.12 Documentation, Dassault Systèmes, Providence, USA, 2014.
- [43] FRANC3D, FRANC3D Reference Manual, Fracture Analysis Consultants Inc., Ithaca, USA, 2016.
- [44] R. Nahta, B. Moran, Domain integrals for axisymmetric interface crack problems, International Journal of Solids and Structures 30 (1993) 2027–2040.
- [45] C. Busse, D. Gustafsson, P. Rasmusson, B. Sjödin, J. Moverare, K. Simonsson, D. Leidermark, Three-Dimensional LEFM Prediction of Fatigue Crack Propagation in a Gas Turbine Disk Material at Component Near Conditions, Journal of Engineering for Gas Turbines and Power 138 (2016).